

Article

Replacement of Cobalt in Lithium-Rich Layered Oxides by n-Doping: A DFT Study

Mariarosaria Tuccillo^{1,2}, Lorenzo Mei¹, Oriele Palumbo², Ana Belén Muñoz-García^{3,4}, Michele Pavone^{4,5}, Annalisa Paolone² and Sergio Brutti^{1,2,4,*}

- ¹ Department of Chemistry, University of Rome La Sapienza, Piazzale Aldo Moro 5, 00185 Rome, Italy; mariarosaria.tuccillo@uniroma1.it (M.T.); mei.1810227@studenti.uniroma1.it (L.M.)
- ² Consiglio Nazionale delle Ricerche, Istituto dei Sistemi Complessi, Piazzale Aldo Moro 5, 00185 Rome, Italy; oriele.palumbo@roma1.infn.it (O.P.); annalisa.paolone@roma1.infn.it (A.P.)
- ³ Department of Physics E. Pancini, University of Naples Federico II, Via Cintia 21, 80126 Napoli, Italy; anabelen.munozgarcia@unina.it
- ⁴ GISEL-Centro di Riferimento Nazionale per i Sistemi di Accumulo Elettrochimico di Energia, INSTM Via G. Giusti 9, 50121 Firenze, Italy; michele.pavone@unina.it
- ⁵ Department of Chemical Sciences, University of Naples Federico II, Via Cintia 21, 80126 Napoli, Italy
- * Correspondence: sergio.brutti@uniroma1.it

Featured Application: Environmentally friendly positive electrode materials for high-capacity lithium-ion batteries.

Abstract: The replacement of cobalt in the lattice of lithium-rich layered oxides (LRLO) is mandatory to improve their environmental benignity and reduce costs. In this study, we analyze the impact of the cobalt removal from the trigonal LRLO lattice on the structural, thermodynamic, and electronic properties of this material through density functional theory calculations. To mimic disorder in the transition metal layers, we exploited the special quasi-random structure approach on selected supercells. The cobalt removal was modeled by the simultaneous substitution with Mn/Ni, thus leading to a p-doping in the lattice. Our results show that cobalt removal induces (a) larger cell volumes, originating from expanded distances among stacked planes; (b) a parallel increase of the layer buckling; (c) an increase of the electronic disorder and of the concentration of Jahn–Teller defects; and (d) an increase of the thermodynamic stability of the phase. Overall p-doping appears as a balanced strategy to remove cobalt from LRLO without massively deteriorating the structural integrity and the electronic properties of LRLO.

Keywords: density functional theory; Li-ion batteries; positive electrodes; lithium-rich layered oxides; cobalt



Citation: Tuccillo, M.; Mei, L.; Palumbo, O.; Muñoz-García, A.B.; Pavone, M.; Paolone, A.; Brutti, S. Replacement of Cobalt in Lithium-Rich Layered Oxides by n-Doping: A DFT Study. *Appl. Sci.* **2021**, *11*, 10545. <https://doi.org/10.3390/app112210545>

Academic Editor: Young-Kyu Han

Received: 8 October 2021

Accepted: 5 November 2021

Published: 9 November 2021

Publisher's Note: MDPI stays neutral with regard to jurisdictional claims in published maps and institutional affiliations.



Copyright: © 2021 by the authors. Licensee MDPI, Basel, Switzerland. This article is an open access article distributed under the terms and conditions of the Creative Commons Attribution (CC BY) license (<https://creativecommons.org/licenses/by/4.0/>).

1. Introduction

Lithium-ion batteries are a power source widely used for numerous applications, including electric vehicles (EVs), computer and consumer electronic products, and energy storage devices for renewable and smart grids [1–4]. Current cathode materials used in Li-ion batteries, as LiCoO₂ and LiM₂O₄, suffer from lower-than-desired capacity and structural instability during cycling, which limits their lifetime [5–9].

Over-stoichiometric Li-rich nickel-manganese-cobalt layered oxides (LRLO, lithium-rich layered oxides) are a family of promising positive electrode materials with a general formula Li[Li_xM_{1-x}]O₂ (with M= transition metal blend) characterized by an over-stoichiometric lithium content, thus implying the simultaneous presence in the same crystallographic site of a mixture of transition metals and lithium atoms (TM atomic sites) [7,10–12]. These materials have a sluggish and ambiguous crystal structure [5,13–15], where two similar layered lattices are integrated [16]. The first structure crystallizes in a Li₂MnO₃ monoclinic prototype (mC24, easily rewritten as Li[Li_{1/3}Mn_{2/3}]O₂; Li in 2c and 4h

with $y = 0.6606$; O in 4i with $x = 0.2189$ and $z = 0.2273$, and 8j with $x = 0.254$ $y = 0.32119$ and $z = 0.2233$; TM in 2b and 4g with $y = 0.16708$) with a $C2/m$ symmetry, whereas the second one crystallizes in a α - NaFeO_2 -prototype and adopts an $R3^-m$ symmetry (hR12, Li in 3b, TM in 3a and O in 6c with $x = 0.7458$) [17–19]. Both lattices stack a repeated motif constituted by four parallel layers containing Li, O, TM, and O atomic species (where TM stands for a blend of transition metal ions and lithium ions), respectively, and differ by the local mutual arrangements of the TMO_6 and LiO_6 octahedra, as well as in the layers' stacking sequence. A full randomization among transition metals and lithium ions on the TM layers, and stacking faults along the layer-piling direction make the two hR12 and a mC24 structures indistinguishable [20], thus suggesting that local fluctuations in the defect concentrations can induce the coexistence of the two symmetries.

Overall, the compresence of hexagonal and monoclinic symmetries in LRLO has been proved experimentally but an effective phase separation is debatable [17–19]. As an example, Jarvis et al. proposed, based on experimental evidence, that $\text{Li}[\text{Li}_{0.2}\text{Mn}_{0.6}\text{Ni}_{0.2}]\text{O}_2$ is a single-phase hR12 solid solution with a partial long range lithium ordering, leading to a mC24-like superlattice [21]. On the other hand, Gu et al. proved that the same layered material with stoichiometry $\text{Li}[\text{Li}_{0.2}\text{Mn}_{0.6}\text{Ni}_{0.2}]\text{O}_2$ is a nanoscale composite cathode where hR12 and mC24 domains coexist [22]. An interesting hypothesis has been proven by Bareño et al., who investigated the long range and local structure of $\text{Li}_{1.2}\text{Co}_{0.4}\text{Mn}_{0.4}\text{O}_2$, suggesting that the LRLO material is constituted by a dendritic microstructure of hR12 and mC24 phases where Mn^{4+} and Co^{3+} are preferentially segregated in monoclinic and hexagonal lattices, respectively [16].

LRLO materials with a variety of compositions can exchange large specific capacity in lithium half cells ($\sim 250 \text{ mAh g}^{-1}$) at high working potentials (3.5–3.9 V vs. Li) [7,10–12], thanks to the combination of the redox reactions of transition metals, e.g., $\text{Mn}^{3+/4+}$, $\text{Ni}^{2+/3+/4+}$, $\text{Co}^{3+/4+}$, etc., and the anionic oxo/peroxo redox activity (i.e., $(\text{O}_2^{4-})/(\text{O}_2^{2-})$) [23,24]. Unfortunately, the oxygen-mediated lithium exchange mechanism promotes the inevitable release of gaseous O_2 at high potentials [25], and the formation of oxygen vacancies. The accumulation of these point defects leads to structural distortions upon cycling [26,27], and to a monotonic decay in the electrode performance [28,29].

A possible way to mitigate the structural rearrangements in LRLO is the incorporation in the transition metal blend of redox inactive metals, such as Al, Zr, Ti [30–32], or the substitution Li^+ with other alkali cations, e.g., K and Na [33]. Aside from these research trends, the search of innovative LRLO must tackle the challenge of the reduction of the cobalt content. In fact, cobalt removal in positive electrode materials for batteries has been identified by the EU and DOE [34,35] as a key-goal to improve the environmental benignity of these energy storage device. However, any alteration of the metal blend in the transition metal layer has inevitable effects on the electronic and crystallographic structure of the LRLO, as well as on its thermodynamic stability, thus affecting the resulting battery performance.

Here, we tackle the challenge to investigate the impact of the removal of cobalt on the electronic, crystallographic, and thermodynamic properties of a Li-rich layered oxide material with general formula of $\text{Li}_{1.2}\text{Ni}_{0.2-x/2}\text{Mn}_{0.6-x/2}\text{Co}_x\text{O}_2$ by density functional theory (DFT). We adopted a partially randomized $5 \times 2 \times 5/3$ supercell, built from the hR12 lattice, to explicitly mimic (a) the full atomic disorder on the TM layers, and (b) the occurrence of a stacking fault along the hexagonal c -axis to break the local hR12 lattice symmetry [16]. Our aim is to draw a comprehensive picture of the impact of the p -doping, indirectly induced by the substitution of cobalt with manganese and nickel, on a realistic LRLO lattice, without relevant constraints on symmetries.

First principles modeling studies on LRLOs have been reported by Wang et al. [36] and Lo et al. [37], tackling the role of oxygen vacancies and dopant elements on the electronic structure and crystal stability of these partially disordered oxides. In both cases, authors described the transition metal layer using regular alternated motifs among Li/Mn/Co/Ni atomic species to mimic the metal blend. Here, we adopt a different strategy, by applying

the special quasi-random structure (SQS) approach to mimic through a cluster expansion formalism a fully disordered occupancy of the atomic sites in the transition metal layer. Our method allows a realistic representation of disorder without pre-determined structural motifs or postulated clustering of similar atomic species. To our knowledge, this is the first attempt to apply SQS to DFT calculations on LRLOs.

2. Methods

All calculations have been performed with the Vienna Ab-initio Simulation Package (VASP), which performs periodic ab initio quantum mechanical calculations within the Kohn–Sham density functional theory (DFT) [38,39] framework, with projector-augmented wave potentials and plane wave basis sets. We applied the generalized-gradient approximation (GGA) [40] in the spin polarized case with the exchange-correlation density functional by Perdew, Burke, and Ernzenhof (PBE) [41].

We used the DFT + U method [42,43], which has been extensively validated for correcting the large self-interaction error in transition metal oxides [41], caused by the approximate form of standard exchange-correlation density functional when applied to strongly localized unpaired electrons, such as in the d manifold of Co, Ni, and Mn. An effective value of $U-J = 4.00$ eV has been used for all Co, Ni, and Mn d electrons. This value is an average between the values of Co, Mn, and Ni, reported from ab-initio UHF calculations, and has been recently validated by us for LiMO_2 layered phases ($M = \text{Co, Ni, Mn}$) [44–46]. We used a kinetic energy cut-off of 520 eV and Brillouin Zone sampled at the Gamma point. We optimized the structural parameters of supercells by iteratively relaxing the ion positions and the cell lattices without any symmetry constraints until the residual force on each atom was <0.01 eV \AA^{-1} . Bader charge analysis [47] was performed on the all-electron charge density files (the core density was generated from the pseudo-potential files) [48,49]. Magnetic moments have been obtained as a direct output of the spin polarized calculations, using the computational routines embed in the VASP code.

The structures of four Li-rich layered oxides with the general formula $\text{Li}_{1.2}\text{Ni}_{0.2-x}/2\text{Mn}_{0.6-x/2}\text{Co}_x\text{O}_2$ and different Co contents (i.e., $x = 0.12, 0.08, 0.04,$ and 0 , namely LNMC12, LNMC08, LNMC04, and LNM) have been built starting from the hR12 prototype unit cell, and using a $5 \times 2 \times 5/3$ supercell. The final supercell contains 200 atoms ($\text{Li}_{50}(\text{Li}_{10}\text{Ni}_{10}\text{Mn}_{30})\text{O}_{100}$ for the LNM stoichiometry) stacked in 20 layers, obtained by 5 repetitions along the c-axis of the stacking of a Li/O/TM/O parallel planes motif. Li and O planes are constituted only by oxygen and lithium atoms, respectively, whereas in TM planes there is the simultaneous presence of nickel, manganese, cobalt, and lithium atoms. The four modeled supercells with different Co contents are shown in Figure 1. The tables with atomic positions and the supercell unit axes matrix are reported in the Supplementary Information (SI), Tables S1–S3.

To model transition metal disorder in multicomponent TM layers in the LNM supercell, we have adopted the special quasi-random structure (SQS) approach [50,51]: this method allows for the modeling of a random solid solution in a supercell of the desired size by mimicking random correlation functions up through nearest-neighbor, next-nearest-neighbor interactions, and so on. The SQS method relies on the cluster expansion (CE) formalism proposed by Mayer [52]. We used the ATAT suite (alloy-theoretic automated toolkit) that exploits an SQS-based algorithm in search for a fully randomized distribution of Ni, Mn, and Li ions in the TM layers within the LNM supercell [53].

Starting from the fully randomized LNM lattice ($\text{Li}_{50}(\text{Li}_{10}\text{Ni}_{10}\text{Mn}_{30})\text{O}_{100}$), the other supercells with different Co contents have been obtained by point doping: (LNMC4) 2 Co to replace 1 Ni and 1 Mn ($\text{Li}_{50}(\text{Li}_{10}\text{Ni}_9\text{Mn}_{29}\text{Co}_2)\text{O}_{100}$); (LNMC8) 4 Co to replace 2 Ni and 2 Mn ($\text{Li}_{50}(\text{Li}_{10}\text{Ni}_8\text{Mn}_{28}\text{Co}_4)\text{O}_{100}$); and (LNMC12) 6 Co to replace 3 Ni and 3 Mn ($\text{Li}_{50}(\text{Li}_{10}\text{Ni}_7\text{Mn}_{27}\text{Co}_6)\text{O}_{100}$), respectively. To identify the most stable supercell for each cobalt concentration, among the innumerable possible structures, we compared the energy stability of selected configurations. As an example, we discuss the identification of the LNMC4 minimal energy supercell.

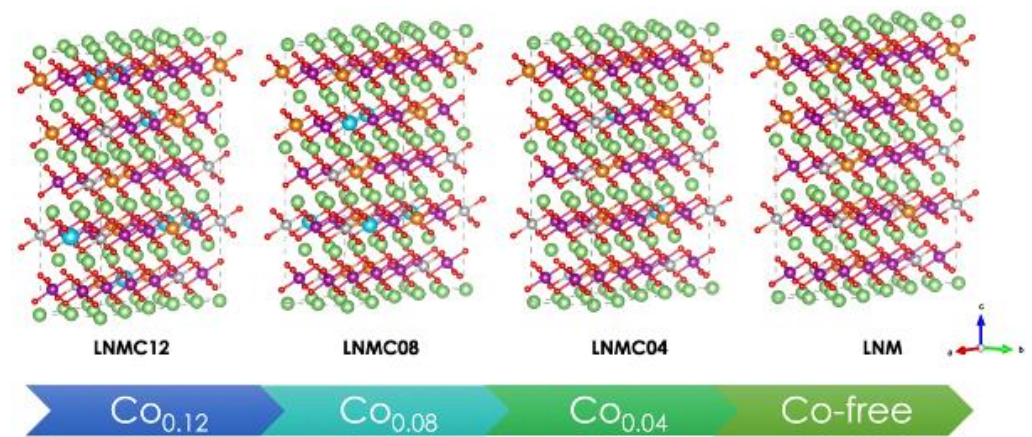


Figure 1. Optimized geometry and volume structures supercell $5 \times 2 \times 5/3$ containing 200 atoms. On the left, $\text{Li}_{1.2}\text{Ni}_{0.14}\text{Mn}_{0.54}\text{Co}_{0.12}\text{O}_2$ (LPMC12). In the middle, $\text{Li}_{1.2}\text{Ni}_{0.16}\text{Mn}_{0.56}\text{Co}_{0.08}\text{O}_2$ (LPMC08), and $\text{Li}_{1.2}\text{Ni}_{0.18}\text{Mn}_{0.58}\text{Co}_{0.04}\text{O}_2$ (LPMC04). On the right $\text{Li}_{1.2}\text{Ni}_{0.2}\text{Mn}_{0.6}\text{O}_2$ (LNM). Color code: Li light green; Li/TM orange; Ni grey; Mn purple; Co light blue; and O red.

The randomized LNM supercell has been fully relaxed to its energy minimum with respect to cell parameters and atomic positions. As a first step, we have built three LPMC4 supercell configurations by point substitution of Mn/Ni pairs, where cobalt atoms are near (two Co on the same TM layer), intermediate (two Co on subsequent TM layers), or diluted (two Co on TM layers separated by a Li layer), as shown in Figure S1 of the SI. We have compared the near-intermediate-diluted configurations relative stabilities by running full self-consistent field relaxations of the electron densities. Once established the energetic similarity of the diluted and intermediate configurations, we have discarded the near configuration that is less stable. As a second step, we have compared the relative stability of all inequivalent diluted and intermediate configurations, with respect to the local six vicinal atoms on the TM layer surrounding each cobalt substituent (i.e., Mn, Ni, or Li atoms in various amounts, depending on the randomization), as shown in the SI, Figure S2. The configuration with the minimal energy has been adopted and further relaxed in respect with cell parameters and atomic positions. Following a similar method, we identified the lowest energy configuration for LPMC08 and LPMC12.

3. Results

3.1. Crystal Structures of Cobalt Doped LRLO

Despite the absence of constraints during structural relaxations, all supercells keep the hexagonal symmetry without any distortion and the layered structure, in line with the experimental evidence [54–57]. Thus, starting from each optimized supercell, we evaluated the hexagonal hR12-apparent lattice parameters for all cobalt concentrations, using the $[5 \times 2 \times 5/3]^{-1}$ inverse supercell transformation.

In the Table 1, we compare the calculated values with those available in the literature (reported in parentheses) [54]. The cell parameters agree within 1.5%, with respect to experiments for both LNM and LPMC4 stoichiometries, thus confirming the accuracy of our modeling.

Overall, the substitution of cobalt in the supercell leads to an isotropic expansion of both *a* and *c* cell parameters, and, therefore, of the cell volume: this trend is in excellent quantitative agreement with the available experimental literature [55,56]. Remarkably, the volume increase observed passing from LPMC12 to LPMC8 and LPMC4 does not occur in passing from LPMC4 to the Co-free LNM supercell, where a slight cell volume shrinking of -0.06% is observed. Despite the LPMC4 stoichiometry having been studied for application in Li-ion batteries [57], we lack an experimental confirmation of this last structural peculiarity.

Table 1. Hexagonal hR12-reduced cell parameters of the optimized supercells. Available experimental literature values are reported in parentheses [54,56,58].

	Supercells			
	LNMC12	LNMC08	LNMC04	LNM
a (Å)	2.893	2.902 (2.874)	2.907	2.907 (2.893)
c (Å)	14.430	14.477 (14.28)	14.500	14.498 (14.292)
V (Å ³ /f.u.)	34.87	35.21 (34.24)	35.38	35.36 (34.72)
$\alpha = \beta$ (°)	90	90	90	90
γ (°)	120	120	120	120
a/c	0.200	0.200	0.200	0.200

Focusing on the alteration of the layers stacking with the cobalt content, we evaluated the changes in the O-(Li)-O and O-(TM)-O, oxygen-oxygen interlayer average distance, and the out-of-plane corrugations of the various atomic planes.

The O-(TM)-O distances are 2.142, 2.147, 2.151, and 2.151 Å for the LNMC12, LNMC8, LNMC4, and LNM compositions, respectively, whereas the corresponding O-(Li)-O are 2.671, 2.678, 2.685, and 2.682 Å. Thus, both O-(Li)-O and O-(TM)-O interlayer mean distances increase in parallel with the substitution of Co and p-doping of the lattice. The O-(TM)-O expansion can be an indirect clue to the increase of the Ni²⁺/Ni³⁺/Mn³⁺ concentrations originating from the larger Ni content, and a possible presence of Jahn–Teller defects (see below for more details); in fact, all these ions are larger than Mn⁴⁺ and Co³⁺ [59]. On the other hand, the origin of the expansion of the O-(Li)-O distance is less clear. Overall, this effect is expected to be beneficial for the transport of Li⁺ ions across the layer, thanks to the less effective coordination originating from the longer (and weaker) Li-O bonds, while removing Co from the lattice.

Turning to the buckling of the atomic layers, these inevitable corrugations are due to the heterogeneity and fluctuation of the local composition. To evaluate the structural disorder emerging at atomic level in the LRLO structures, we calculated the displacement factors, σ^2 for all fractional atomic position, with respect to a $5 \times 2 \times 5/3$ supercell built from the ordered LiCoO₂ hR12 lattice. We considered the following equation:

$$\sigma^2 = \frac{\sum_{i=1}^N [(x_i - x'_i)]^2 + [(y_i - y'_i)]^2 + [(z_i - z'_i)]^2}{N} \quad (1)$$

where (x_i, y_i, z_i) are the fractional coordinates of each atomic species in the site i within the supercells of the LNMC12, LNMC08, LNMC04, and LNM structures; (x'_i, y'_i, z'_i) are the fractional coordinates of the same atomic site i in the ordered LiCoO₂ supercell; and N is the total number of atoms with the same atomic identity. The displacement factor is an evaluation of the mean buckling of the layers, with respect to the perfectly planar arrangement in the LiCoO₂ lattice. We have calculated mean values of σ^2 for Li, LiTM (lithium ions in the TM layer), Ni, Mn, Co, and O for each composition, as shown in Figure 2.

All atomic species in LRLO supercells show large and similar displacements compared to LiCoO₂, ranging between 0.0029 and 0.00023. In particular, whereas the oxygen displacement is almost constant and insensitive with changes in the cobalt content, differences are observed for all other metals. The reduction of the cobalt content from LNMC12 to LNM increases the displacement of the Li⁺ ions in the lithium layers of approximately 600%, and in the TM layers (+770%). Similar increases are observed also for Ni (+594%) and Mn (+450%). On passing, it is interesting to observe that passing from LNMC4 to LNM the buckling of all atomic species seems to slightly decrease. Therefore, the LNMC4 composition shows the mostly buckled layers among all supercells.

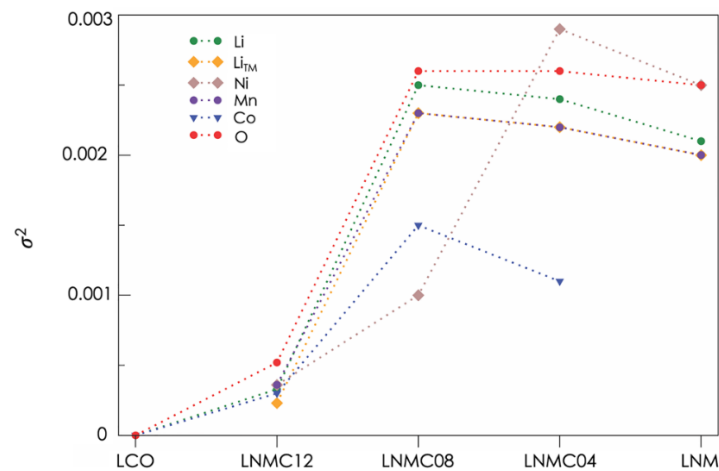


Figure 2. Mean (a-dimensional) displacements factors σ^2 calculated on fractional coordinates for each atomic species in LNMC12, LNMC08, LNMC04, and LNM supercells.

In summary, the removal of cobalt and the simultaneous p-doping of the LRLO lattice induce larger cell volumes, originating from expanded distances among stacked planes, and a parallel increase of the layer buckling.

Turning to the interatomic bonds, we analyzed the distances between transition metals and the first neighbor's oxygen atoms $d_{\text{M-O}}$: all transition metals are surrounded by six oxygen atoms, forming distorted octahedra. The distribution of the M-O (M = Ni, Mn, and Co) bond distances is shown in Figure 3 in the form of Pair Distribution Functions (PDFs).

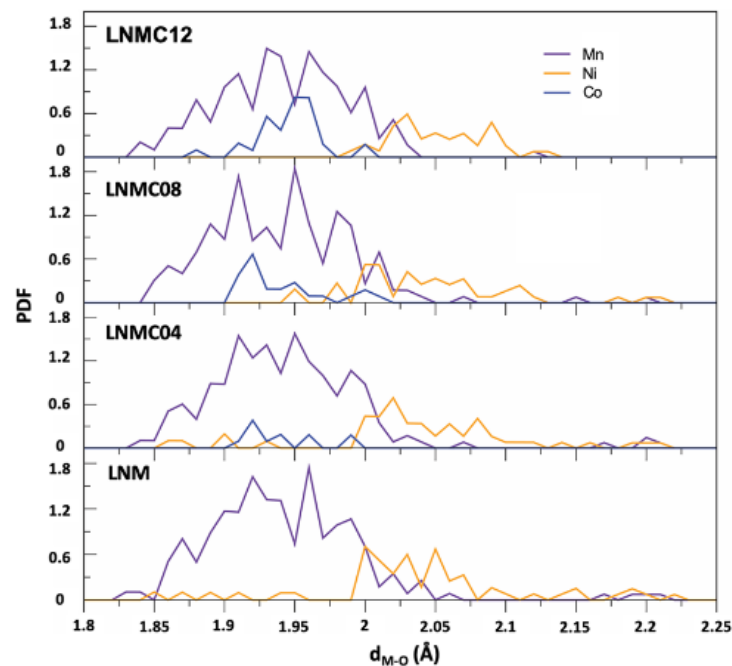


Figure 3. Pair Distribution Functions (PDFs) of LNMC12 (upper panel), LNMC08 (middle panel), LNMC04 (middle panel), and LNM (bottom panel) for Mn-O, Ni-O, and Co-O bond distances.

Qualitatively PDFs are similar for all compositions, being that MnO_6 octahedra very close in dimensions to the CoO_6 , whereas NiO_6 octahedra are larger. The reduction of the cobalt content from LNMC12 to LNM leads to a slight monotonic increase in the Mn-O bond distances, from 1.949 Å to 1.951 Å, as well as a slight decrease for Ni-O, from 2.058 Å to 2.048 Å. It is remarkable to observe that the reduction of cobalt in the structure occurs in parallel with the sparse elongation/compression of few Ni-O and Mn-O bonds. This

may be a clue of the appearance/increase of Jahn–Teller distortions in the LRLO lattices induced by the substitution of Co with a blend of Mn/Ni (see below for more details and discussions in the electronic structure section) [60].

3.2. Electronic Structure of the LRLOs

The electronic structures in terms of density of states for LNM C12, LNM C08, LNM C04, and LNM are shown in Figure 4.

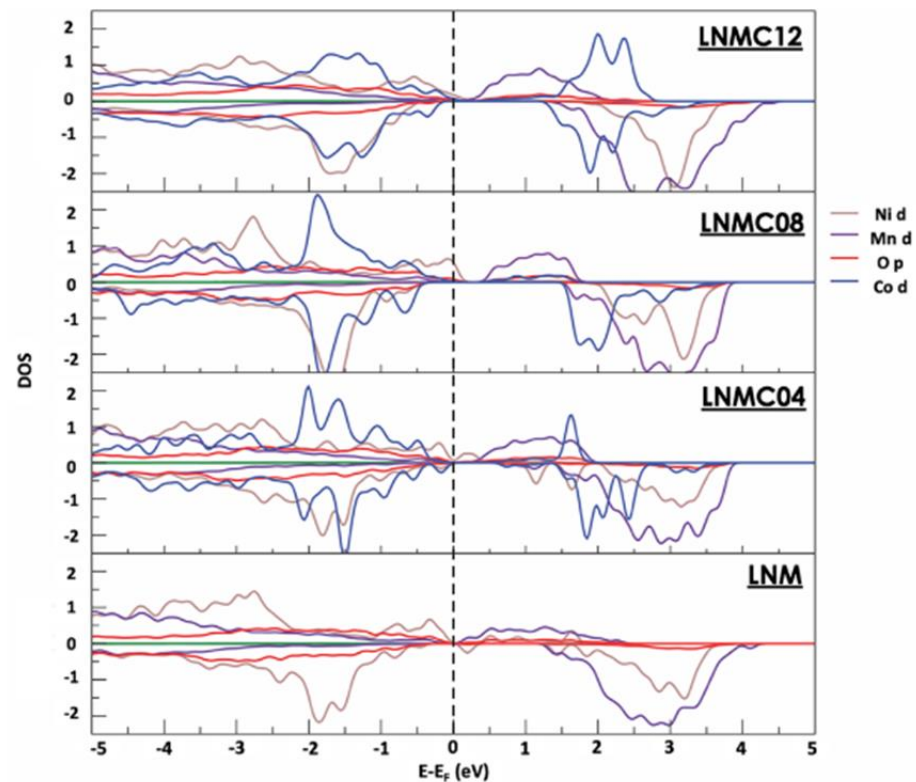


Figure 4. Atomic orbital projected density of states of LNM C12 (upper panel), LNM C08 (upper/middle panel), LNM C04 (middle/bottom panel), which presents a 0-bandgap, and LNM (bottom panel).

First, we can observe a similar metallic character for all Co-containing compositions, whereas the LNM Co-free supercell shows a 0-bandgap character. This change in the electronic structure induced by the complete removal of cobalt from the LRLO lattice agrees with the enhancement of the electronic conductivity obtained by Co doping reported in the literature [61].

Second, a strong hybridization of Ni d states and Mn d states at the Fermi energy with the p-states of the oxygen anions is observed for all supercells, being that the energy distribution of the Ni states is highly distorted by the reduction in the cobalt content.

The analysis of the magnetic moments of the metals allows us to shed light on the oxidation states in the lattices. The mean magnetic moments are:

- Co sites: 0.00 μ_B , for LNM C12, LNM C08, and LNM C04;
- Ni sites of 1.649 μ_B , 1.609 μ_B , 1.521 μ_B , 1.489 μ_B for LNM C12, LNM C08, LNM C04, and LNM respectively;
- Mn sites of 3.199 μ_B , 3.216 μ_B , 3.236 μ_B , 3.239 μ_B for LNM C12, LNM C08, LNM C04, and LNM respectively.

Magnetic moments confirm the qualitative results obtained by PDOS.

The magnetic moments suggest that all Co ions are in 3+ oxidation state in low spin (LS) electronic configuration, $t_{2g}^6 (|\uparrow\downarrow|\uparrow\downarrow|\uparrow\downarrow|) e_g^0 (| | |)$ in all supercells. On the

contrary, the monotonic reduction of the magnetic moments of Ni ions in parallel with the Co substitution suggests a decrease in the concentration of nickel ions in the 2+ oxidation states in the LS electronic configuration $t_{2g}^6 (|\uparrow\downarrow|\uparrow\downarrow|\uparrow\downarrow|) e_g^2 (|\uparrow|\uparrow|)$, and an increase in the fraction of nickel ions in the 3+ oxidation state in the LS electronic configuration, $t_{2g}^6 (|\uparrow\downarrow|\uparrow\downarrow|\uparrow\downarrow|) e_g^1 (|\uparrow|\uparrow|)$. In parallel, an analogue increase in the magnetic moment on Mn is the clue of the decrease in the concentration of manganese ions in the 4+ oxidation state in the HS electronic configuration, $t_{2g}^3 (|\uparrow|\uparrow|\uparrow|) e_g^0 (| | |)$, and an increase in the fraction of manganese ions in the 3+ oxidation state in the HS electronic configuration, $t_{2g}^3 (|\uparrow|\uparrow|\uparrow|) e_g^1 (|\uparrow|\uparrow|)$. The molar fractions of 3+ ions are shown in the SI (Table S5) for all compositions. Previous experimental X-ray absorption analysis of the oxidation states of Mn and Ni for the same LMN Co-free composition agrees with our evaluations, thus confirming the contemporary presence of Ni^{3+} , Ni^{2+} , Mn^{3+} , and Mn^{4+} in the structure [62]. This analysis is also confirmed by the computed Bader charges show in Figure S4 in the SI, that confirm the increase of the Ni^{3+} and Mn^{3+} concentrations in parallel with the Co substitution.

Due to their electronic configurations, Ni^{3+} and Mn^{3+} are Jahn–Teller ions (JT) [60]. The representation of selected CoO_6 , NiO_6 , and MnO_6 octahedra is shown in Figure 5, where the JT distortions are highlighted. Co^{3+} ions are not JT ions, and therefore all CoO_6 bond distortions are induced by the different chemical environment of TM-layers.

Jahn-Teller Distortions					
	LNMC12	LNMC08	LNMC04	LNM	
Mn^{3+} :					
Ni^{3+} :					
No Jahn-Teller Distortions					
	LNMC12	LNMC08	LNMC04	LNM	
Mn^{4+} :					
Ni^{2+} :					
Co^{3+} :					

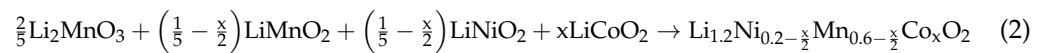
Figure 5. JT distorted and undistorted octahedra in LNMC12, LNMC08, LNMC04, and LNM supercells.

Ni^{3+} and Mn^{3+} are in an octahedral coordination, and therefore the e_g orbitals emerge as a combination between $d_{z^2}/d_{x^2-y^2}$ and oxygen p orbitals. In both $(Ni^{3+})O_6$ and $(Mn^{3+})O_6$ octahedra, the partial occupancy of the e_g orbitals leads to alterations in the oxygen-metal bond lengths: usually, the axial bond length increases, whereas the four equatorial bond lengths decrease [63]. Our calculations correctly highlight the JT-distortions in the LNMC12, LNMC08, LNMC04, and LNM structures.

It is remarkable to observe the four times larger JT distortion concentration in the Co-free LNM lattice, compared to the LNMC12 one (Table S5 of the SI). Apparently, cobalt ions act as electronic disorder “modulators”, and their substitution induces an increase in local octahedral distortions due to JT defects. According to literature, the increase of JT distortions hinders the lattice stability during the lithiation and de-lithiation process, as they can facilitate phase segregations and structural transitions [64–66]. In this respect, the n-doping strategy here proposed is unable to fully suppress the JT disorder induced by the Co removal. However, as far as we know, this is the first ever reported quantitative evaluation of the JT distortions occurring upon Co substitution in LRLO lattices, and is a benchmark for further studies.

3.3. Phase Stability of LRLO

The thermodynamic stability of the LRLO supercells have been evaluated by calculating the energy of formation from the ternary ordered Li-metal oxides. Considering a generic LRLO material with stoichiometry $\text{Li}_{1.2}\text{Ni}_{0.2-x/2}\text{Mn}_{0.6-x/2}\text{Co}_x\text{O}_2$, we evaluated the thermodynamics of the following general reaction for the four supercells:



The corresponding equation for the formation energy at 0K, $\Delta_{\text{form}}E_{0\text{K}}$, of a an LRLO with fixed x and general formula $\text{Li}_{1.2}\text{Ni}_{0.2-x/2}\text{Mn}_{0.6-x/2}\text{Co}_x\text{O}_2$ (LNMCx) is given by Equation (3):

$$\Delta_{\text{form}}E_{0\text{K}}(2) = E_{\text{tot,LNMCx}} - (0.4 E_{\text{tot,Li}_2\text{MnO}_3} + 0.2 - x/2 E_{\text{tot,LiMnO}_2} + 0.2 - x/2 E_{\text{tot,LiNiO}_2} + x E_{\text{tot,LiCoO}_2}) \quad (3)$$

where x is the stoichiometric coefficient (0.12, 0.08, 0.04, and 0), and E_{tot} values are the electronic total energies calculated at the DFT+U level of each species. The thermodynamic properties of Li_2MnO_3 , LiMnO_2 , LiCoO_2 , and LiNiO_2 have been evaluated by us in a previous work at the same level of theory [46]. We can approximate formation energy at 0K with the standard formation enthalpy at 0 K, i.e., $\Delta_{\text{form}}E_{0\text{K}} \approx \Delta_{\text{form}}H^{\circ}_{0\text{K}}$. This approximation, i.e., we neglect the variation of the zero-point vibrational contributions, is expected to be small, since it is given by the algebraic difference between zero-point energies of the product and reagents, as defined in Equation (2).

For each LRLO, we also evaluated the configurational entropy S_{conf} for the four LNMCx stoichiometries following Equation (4):

$$S_{\text{conf,LNMCx}} = R ((0.2 - x/2)\ln(0.2 - x/2) + x \ln(x) + (0.6 - x/2) \ln(0.6 - x/2) + 0.2 \ln(0.2)) \quad (4)$$

where R is the gas constant. Being that the structures of the Li_2MnO_3 , LiMnO_2 , LiCoO_2 , and LiNiO_2 ternary oxides constituted fully ordered lattices, the corresponding configurational entropies are null. As a consequence, the configurational entropy variation of reactions (2), i.e., $\Delta_r S_{\text{conf,LNMCx}}$, are equal to the configurational entropies of the four LNMCx lattices. By considering the third law of thermodynamics, we can calculate the standard entropy of formation reactions (2) at 0K with the corresponding variation of the configurational entropy:

$$\Delta_{\text{form}}S^{\circ}_{0\text{K}}(E2) \approx \Delta_r S_{\text{conf,LNMCx}} = S^{\circ}_{\text{conf,LNMCx}} \quad (5)$$

Starting from the here derived standard enthalpy of formation and standard entropy of formation at 0 K for the LNMCx phases from the ternary ordered oxides (see Equation (2)), we have estimated the corresponding standard Gibbs energy of formation at 298 K $\Delta_{\text{form}}G^{\circ}_{298\text{K}}(2)$, by the usual equation $\Delta G = \Delta H - T\Delta S$. The estimate of the $\Delta_{\text{form}}G^{\circ}_{298\text{K}}(2)$ neglects the possible contribution of thermal effects on entropies and enthalpies: this is an unavoidable approximation in the view of the lack of reliable experimental collections of the heat capacities in the 0–298 K temperature range for all phases.

The calculated $\Delta_{\text{form}}H^{\circ}_{0\text{K}}$, $\Delta_{\text{form}}S^{\circ}_{0\text{K}}$ and $\Delta_{\text{form}}G^{\circ}_{298\text{K}}$ for all stoichiometries are listed in Table 2: Gibbs free energy of formation of all LRLO are reported in the SI (Table S6) as a function of the temperature.

Table 2. Thermodynamic data for the LNMC12, LNMC08, LNMC04, and LNM phases.

	Phases			
	LNMC12	LNMC08	LNMC04	LNM
$\Delta_{\text{form}}H^{\circ}_{0\text{K}}/\text{eV at}^{-1}$	−0.040	−0.044	−0.054	−0.079
$\Delta_{\text{form}}S^{\circ}_{0\text{K}}/\text{eV at}^{-1} \text{ K}^{-1}$	$1.02 \cdot 10^{-4}$	$9.9 \cdot 10^{-5}$	$9.3 \cdot 10^{-5}$	$8.2 \cdot 10^{-5}$
$\Delta_{\text{form}}G^{\circ}_{298\text{K}}/\text{eV at}^{-1}$	−0.070	−0.073	−0.082	−0.103

The formation Gibbs energies of the LRLO phases are more negative while decreasing Co content, despite the parallel increase in the structural disorder, i.e., atomic displacement, and electronic disorder, i.e., large concentration of JT defects. This trend is driven by enthalpy and is likely due to the formation of stronger chemical bonds in the structure, whereas the stabilization from the configurational entropy unavoidably decreases while reducing the amount of cobalt. Thus, the p-doping of the LRLO lattice, induced by the simultaneous substitution of Co atoms with Mn and Ni, alters the stability of the disordered lattice.

To shed further light on the LNMCx phase diagram, we evaluated the excess standard Gibbs energy of formation of the intermediate phases using the data in Table S6. The excess standard Gibbs energy of formation at temperature T for the phase j containing x moles of Co in the $\text{Li}_{1.2}\text{Ni}_{0.2-x/2}\text{Mn}_{0.6-x/2}\text{Co}_x\text{O}_2$ formula ($\Delta_{\text{excess}}G^{\circ}_T(j_x)$) is defined by the Equation (6):

$$\Delta_{\text{excess}}G^{\circ}_T(j_x) = \Delta_f G^{\circ}_T(j_x) - \frac{x}{0.12} \Delta_f G^{\circ}_T(\text{LNMC12}) - \frac{0.12-x}{0.12} \Delta_f G^{\circ}_T(\text{LNM}) \quad (6)$$

The $\Delta_{\text{excess}}G^{\circ}_T(j_x)$ represents the relative thermodynamic stability of the LNMC08 and LNMC04 phases, compared to mixtures of LNM and LNMC12. The values of the $\Delta_{\text{excess}}G^{\circ}_T(j_x)$ are shown in the form of a thermodynamic phase diagram in the Figure 6 for four different temperatures, namely 298.15, 500, 1000, and 1500 K.

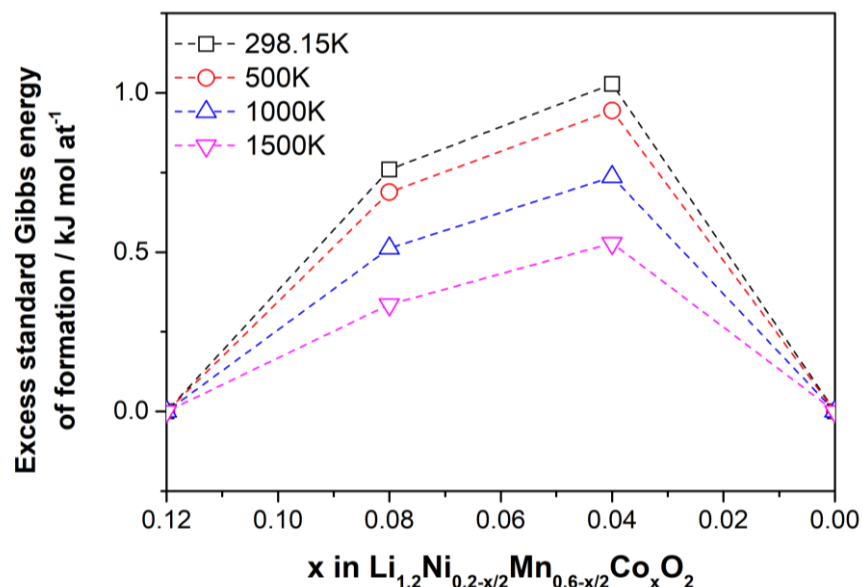


Figure 6. $\Delta_{\text{excess}}G^{\circ}_T(j_x)$ at 298, 500, 1000, 1500 K for the intermediate LNMCx materials.

Remarkably, the $\Delta_{\text{excess}}G^{\circ}_T(j_x)$ is positive at all temperatures for both LNMC08 and LNMC04; this trend suggests that the formation of a single phase LRLO in this composition

range is thermodynamically unfavorable. In fact, both LNMC08 and LNMC04 lattices are thermodynamically less stable compared to a balanced mixture of LNM and LNMC12. As a consequence, both LNMC08 and LNMC04 are expected to undergo to a phase separation reaction driven by the larger stability of LNMC12 and LNM phases. On passing we underline that the phase separation reaction is less favorable at high temperatures.

It is important to underline that the formation of single phase LRLO with LNMC08, LNMC04 or similar compositions has been proven in recent experimental reports [54,56,58,67]. In this respect, we can speculate that, despite the unfavorable thermodynamics, the formation of single-phase metastable lattices is likely driven by crystal growth kinetics and the formation of defects (e.g., stacking faults, antisites, dislocations). In particular, extended defectivities can easily alter the overall thermodynamics thus extending the complexity of these systems.

On passing, it is important to underline that our thermodynamic evaluations of the fully lithiated LRLO do not necessarily imply a parallel landscape in the thermodynamic properties of de-lithiated phases. In this respect, thermodynamic studies about the stability of LRLO upon de-lithiation are necessary to fully understand the interplay between Co removal and battery performance.

4. Conclusions

In this work, we have investigated using firsts principles methods based on DFT, four TM oxide layered materials with a general stoichiometry $\text{Li}_{1.2}\text{Ni}_{0.2-x/2}\text{Mn}_{0.6-x/2}\text{Co}_x\text{O}_2$, considering different Co contents: LNMC12, LNMC08, LNMC04, and LNM with $x = 0.12, 0.08, 0.04$, and 0 , respectively. We have addressed structural, electronic, and thermodynamic properties for each material to describe the impact of Co substitution by Mn/Ni and the parallel p-doping of the lattice. Our analysis describes in detail the structural features of all compositions, their relative stabilities, and their electronic properties, in terms of band gap, oxidation state of the transition metal and JT distortion. The obtained description of the bonding and structural properties of the modelled structures is in good agreement with the available experimental literature.

Overall, reduction in the Co content in the LRLO lattice on the one hand leads to an expansion of the structures due to the greater electronic distortions. This structural effect can promote the mobility of lithium ions, thanks to the weaker coordination. However, the number of electronic states at the Fermi level decreases, possibly negatively impacting the electronic conductivity. These trends occur in parallel with the alteration of the thermodynamic stability of the lattices, while removing cobalt. In this view, the p-doping strategy provided by the Mn/Ni simultaneous incorporation appears as a balanced way to remove cobalt from the lattice without massively degrading the structural and electronic properties of the LRLO.

Supplementary Materials: The following are available online at <https://www.mdpi.com/article/10.3390/app112210545/s1>, Figure S1: Different Co distribution in different layers: diluted in which Co atoms are separated by two Li-layers and one TM-layer; intermediate, in which Co atoms are separated by one Li-layers; near, in which Co atoms are in same TM-layer. On the left a qualitative energy diagram of ΔE between diluted, intermediate and near distribution. Figure S2: Different Co configuration for diluted and intermediate distribution, considering Co chemical environments. Table S1: Fractional Coordinate of LNM. Table S2: Fractional Coordinate of LNMC04. Table S3: Fractional Coordinate of LNMC08. Table S4: Fractional Coordinate of LNMC12. Figure S3: Pair Distribution Function (PDF) of LNMC12 (upper panel), LNMC08 (middle panel), LNMC04 (middle panel) and LNM (bottom panel) for Li-O bond distances. Table S5: Mole fraction of JT distortions with respect to: all TMs (χ_{JT}), Ni ions ($\chi_{Ni^{3+}}$) and Mn ions ($\chi_{Mn^{3+}}$) for LNMC12, LNMC08, LNMC04 and LNM. Figure S4: Accumulative differences of Bader charges of Ni and Mn, considering the variation from LNMC12 to LNM; negative Δq implicates a reduction ($\text{Mn}^{4+} \rightarrow \text{Mn}^{3+}$), positive Δq implicates an oxidation ($\text{Ni}^{2+} \rightarrow \text{Ni}^{3+}$). Table S6: Gibbs energy of formation ($\Delta_{\text{form}} G^\circ_{298\text{K}}/\text{kJ mol}^{-1}$) of the LRLO as a function of the temperature.

Author Contributions: Conceptualization, S.B., O.P., A.P.; methodology, A.B.M.-G., M.P.; investigation, M.T., L.M.; writing—original draft preparation, S.B., M.T.; writing—review and editing, A.B.M.-G., M.P., O.P., A.P. All authors have read and agreed to the published version of the manuscript.

Funding: The authors would like to acknowledge the financial support from the European Union Horizon 2020 research and innovation program within the Si-DRIVE project; grant agreement No. 814464.

Institutional Review Board Statement: Not applicable.

Informed Consent Statement: Not applicable.

Data Availability Statement: Data are available upon request to the corresponding author.

Acknowledgments: Arcangelo Celeste and Laura Silvestri are acknowledged for the fruitful discussions.

Conflicts of Interest: The authors declare no conflict of interest.

References

1. Whittingham, M.S. Introduction: Batteries. *Chem. Rev.* **2014**, *114*, 11413. [[CrossRef](#)] [[PubMed](#)]
2. Burke, M.J.; Stephens, J. Political power and renewable energy futures: A critical review. *Energy Res. Soc. Sci.* **2018**, *35*, 78–93. [[CrossRef](#)]
3. Budde-Meiwes, H.; Drillkens, J.; Lunz, B.; Muennix, J.; Rothgang, S.; Kowal, J.; Sauer, D.U. A review of current automotive battery technology and future prospects. *Proc. Inst. Mech. Eng. Part D J. Automob. Eng.* **2013**, *227*, 761–776. [[CrossRef](#)]
4. Hossain, E.; Faruque, H.; Sunny, S.H.; Mohammad, N.; Nawar, N. A Comprehensive Review on Energy Storage Systems: Types, Comparison, Current Scenario, Applications, Barriers, and Potential Solutions, Policies, and Future Prospects. *Energies* **2020**, *13*, 3651. [[CrossRef](#)]
5. Yang, J.; Kim, H.; Ceder, G. Insights into Layered Oxide Cathodes for Rechargeable Batteries. *Molecules* **2021**, *26*, 3173. [[CrossRef](#)] [[PubMed](#)]
6. Hao, G.; Lai, Q.; Zhang, H. Nanostructured Mn-based oxides as high-performance cathodes for next generation Li-ion batteries. *J. Energy Chem.* **2020**, *59*, 547–571. [[CrossRef](#)]
7. Li, Y.; Li, Z.; Chen, C.; Yang, K.; Cao, B.; Xu, S.; Yang, N.; Zhao, W.; Chen, H.; Zhang, M.; et al. Recent progress in Li and Mn rich layered oxide cathodes for Li-ion batteries. *J. Energy Chem.* **2021**, *61*, 368–385. [[CrossRef](#)]
8. Xiao, B.; Omenya, F.; Reed, D.; Li, X. A glance of the layered transition metal oxide cathodes in sodium and lithium-ion batteries: Difference and similarities. *Nanotechnology* **2021**, *32*, 422501. [[CrossRef](#)]
9. Kasnatscheew, J.; Evertz, M.; Kloepsch, R.; Streipert, B.; Wagner, R.; Laskovic, I.C.; Winter, M. Learning from Electrochemical Data: Simple Evaluation and Classification of LiMO₂-type-based Positive Electrodes for Li-Ion Batteries. *Energy Technol.* **2017**, *5*, 1670–1679. [[CrossRef](#)]
10. Foix, D.; Sathiyaraj, M.; McCalla, E.; Tarascon, J.-M.; Gonbeau, D. X-ray Photoemission Spectroscopy Study of Cationic and Anionic Redox Processes in High-Capacity Li-Ion Battery Layered-Oxide Electrodes. *J. Phys. Chem. C* **2016**, *120*, 862–874. [[CrossRef](#)]
11. Saubanère, M.; McCalla, E.; Tarascon, J.-M.; Doublet, M.-L. The intriguing question of anionic redox in high-energy density cathodes for Li-ion batteries. *Energy Environ. Sci.* **2016**, *9*, 984–991. [[CrossRef](#)]
12. Grimaud, A.; Hong, W.T.; Shao-Horn, Y.; Tarascon, J.-M. Anionic redox processes for electrochemical devices. *Nat. Mater.* **2016**, *15*, 121–126. [[CrossRef](#)] [[PubMed](#)]
13. Delmas, C.; Fouassier, C.; Hagenmuller, P. Structural classification and properties of the layered oxides. *Phys. B+C* **1980**, *99*, 81–85. [[CrossRef](#)]
14. Yu, H.; Kim, H.; Wang, Y.; He, P.; Asakura, D.; Nakamura, Y.; Zhou, H. High-energy ‘composite’ layered manganese-rich cathode materials via controlling Li₂MnO₃ phase activation for lithium-ion batteries. *Phys. Chem. Chem. Phys.* **2012**, *14*, 6584–6595. [[CrossRef](#)] [[PubMed](#)]
15. Yu, Z.; Shang, S.-L.; Gordin, M.L.; Mousharraf, A.; Liu, Z.-K.; Wang, D. Ti-substituted Li[Li_{0.26}Mn_{0.6}–xTi_xNi_{0.07}Co_{0.07}]O₂ layered cathode material with improved structural stability and suppressed voltage fading. *J. Mater. Chem. A* **2015**, *3*, 17376–17384. [[CrossRef](#)]
16. Bareño, J.; Balasubramanian, M.; Kang, S.H.; Wen, J.G.; Lei, C.H.; Pol, S.V.; Petrov, I.; Abraham, D.P. Long-Range and Local Structure in the Layered Oxide Li_{1.2}Co_{0.4}Mn_{0.4}O₂. *Chem. Mater.* **2011**, *23*, 2039–2050. [[CrossRef](#)]
17. Yu, H.; Zhou, H. High-Energy Cathode Materials (Li₂MnO₃–LiMO₂) for Lithium-Ion Batteries. *J. Phys. Chem. Lett.* **2013**, *4*, 1268–1280. [[CrossRef](#)]
18. Rozier, P.; Tarascon, J.M. Review—Li-Rich Layered Oxide Cathodes for Next-Generation Li-Ion Batteries: Chances and Challenges. *J. Electrochem. Soc.* **2015**, *162*, A2490–A2499. [[CrossRef](#)]
19. Thackeray, M.M.; Johnson, C.S.; Vaughey, J.T.; Li, N.; Hackney, S.A. Advances in manganese-oxide ‘composite’ electrodes for lithium-ion batteries. *J. Mater. Chem.* **2005**, *15*, 2257–2267. [[CrossRef](#)]

20. Ren, Q.; Xie, H.; Wang, M.; Ding, X.; Cui, J.; Luo, D.; Liu, C.; Lin, Z. Deciphering the effects of hexagonal and monoclinic structure distribution on the properties of Li-rich layered oxides. *Chem. Commun.* **2021**, *57*, 3512–3515. [[CrossRef](#)]
21. Jarvis, K.A.; Deng, Z.; Allard, L.F.; Manthiram, A.; Ferreira, P.J. Atomic Structure of a Lithium-Rich Layered Oxide Material for Lithium-Ion Batteries: Evidence of a Solid Solution. *Chem. Mater.* **2011**, *23*, 3614–3621. [[CrossRef](#)]
22. Gu, M.; Genc, A.; Belharouak, I.; Wang, D.; Amine, K.; Thevuthasan, S.; Baer, D.R.; Zhang, J.-G.; Browning, N.D.; Liu, J.; et al. Nanoscale Phase Separation, Cation Ordering, and Surface Chemistry in Pristine Li_{1.2}Ni_{0.2}Mn_{0.6}O₂ for Li-Ion Batteries. *Chem. Mater.* **2013**, *25*, 2319–2326. [[CrossRef](#)]
23. Kim, I.; Do, J.; Kim, H.; Jung, Y. Charge-transfer descriptor for the cycle performance of β -Li₂MO₃ cathodes: Role of oxygen dimers. *J. Mater. Chem. A* **2020**, *8*, 2663–2671. [[CrossRef](#)]
24. Muhammad, S.; Kim, H.; Kim, Y.; Kim, D.; Song, J.H.; Yoon, J.; Park, J.-H.; Ahn, S.-J.; Kang, S.-H.; Thackeray, M.M.; et al. Evidence of reversible oxygen participation in anomalously high capacity Li- and Mn-rich cathodes for Li-ion batteries. *Nano Energy* **2016**, *21*, 172–184. [[CrossRef](#)]
25. Strehle, B.; Kleiner, K.; Jung, R.; Chesneau, F.; Mendez, M.; Gasteiger, H.; Piana, M. The Role of Oxygen Release from Li- and Mn-Rich Layered Oxides during the First Cycles Investigated by On-Line Electrochemical Mass Spectrometry. *J. Electrochem. Soc.* **2017**, *164*, A400–A406. [[CrossRef](#)]
26. Mohanty, D.; Kalnaus, S.; Meisner, R.A.; Rhodes, K.J.; Li, J.; Payzant, E.; Wood, D.; Daniel, C. Structural transformation of a lithium-rich Li_{1.2}Co_{0.1}Mn_{0.55}Ni_{0.15}O₂ cathode during high voltage cycling resolved by in situ X-ray diffraction. *J. Power Sources* **2013**, *229*, 239–248. [[CrossRef](#)]
27. Gu, M.; Belharouak, I.; Zheng, J.; Wu, H.; Xiao, J.; Genc, A.; Amine, K.; Thevuthasan, S.; Baer, D.R.; Zhang, J.-G.; et al. Formation of the Spinel Phase in the Layered Composite Cathode Used in Li-Ion Batteries. *ACS Nano* **2013**, *7*, 760–767. [[CrossRef](#)]
28. Sathiyaa, M.; Abakumov, A.M.; Foix, D.; Rousse, G.; Ramesha, K.; Saubanere, M.; Doublet, M.-L.; Vezin, H.; Laisa, C.P.; Prakash, A.S.; et al. Origin of voltage decay in high-capacity layered oxide electrodes. *Nat. Mater.* **2014**, *14*, 230–238. [[CrossRef](#)]
29. Croy, J.R.; Gallagher, K.G.; Balasubramanian, M.; Long, B.R.; Thackeray, M.M. Quantifying Hysteresis and Voltage Fade in xLi₂MnO₃•(1-x)LiMn_{0.5}Ni_{0.5}O₂ Electrodes as a Function of Li₂MnO₃ Content. *J. Electrochem. Soc.* **2013**, *161*, A318–A325. [[CrossRef](#)]
30. Nayak, P.K.; Grinblat, J.; Levi, M.; Levi, E.; Kim, S.; Choi, J.W.; Aurbach, D. Al Doping for Mitigating the Capacity Fading and Voltage Decay of Layered Li and Mn-Rich Cathodes for Li-Ion Batteries. *Adv. Energy Mater.* **2016**, *6*, 1502398. [[CrossRef](#)]
31. Dahiya, P.P.; Ghanty, C.; Sahoo, K.; Basu, S.; Majumder, S.B. Suppression of Voltage Decay and Improvement in Electrochemical Performance by Zirconium Doping in Li-Rich Cathode Materials for Li-Ion Batteries. *J. Electrochem. Soc.* **2018**, *165*, A3114–A3124. [[CrossRef](#)]
32. Kam, K.C.; Mehta, A.; Heron, J.T.; Doeff, M.M. Electrochemical and Physical Properties of Ti-Substituted Layered Nickel Manganese Cobalt Oxide (NMC) Cathode Materials. *J. Electrochem. Soc.* **2012**, *159*, A1383–A1392. [[CrossRef](#)]
33. Liu, Y.; Ning, D.; Zheng, L.; Zhang, Q.; Gu, L.; Gao, R.; Zhang, J.; Franz, A.; Schumacher, G.; Liu, X. Improving the electrochemical performances of Li-rich Li_{1.20}Ni_{0.13}Co_{0.13}Mn_{0.54}O₂ through a cooperative doping of Na⁺ and PO₄³⁻ with Na₃PO₄. *J. Power Sources* **2018**, *375*, 1–10. [[CrossRef](#)]
34. Commission Staff Working Document. *Report on Raw Materials for Battery Applications*; JRC118410; Publications Office of the European Union: Luxembourg, 2020. [[CrossRef](#)]
35. Committee of the Regions and the European Investment Bank. *On the Implementation of the Strategic Action Plan on Batteries: Building a Strategic Battery Value Chain in Europe*; European Union, Report number COM(2019) 176; Publications Office of the European Union: Luxembourg; Available online: [https://ec.europa.eu/transparency/documents-register/detail?ref=COM\(2019\)176&lang=en](https://ec.europa.eu/transparency/documents-register/detail?ref=COM(2019)176&lang=en) (accessed on 1 November 2021).
36. Wang, Z.; Lin, X.; Zhang, J.; Wang, D.; Ding, C.; Zhu, Y.; Gao, P.; Huang, X.; Wen, G. Spherical layered Li-rich cathode material: Unraveling the role of oxygen vacancies on improving lithium ion conductivity. *J. Power Sources* **2020**, *462*, 228171. [[CrossRef](#)]
37. Lo, W.-T.; Yu, C.; Leggesse, E.G.; Nachimuthu, S.; Jiang, J.-C. Understanding the Role of Dopant Metal Atoms on the Structural and Electronic Properties of Lithium-Rich Li_{1.2}Ni_{0.2}Mn_{0.6}O₂ Cathode Material for Lithium-Ion Batteries. *J. Phys. Chem. Lett.* **2019**, *10*, 4842–4850. [[CrossRef](#)]
38. Wimmer, E.; Christensen, M.; Eyert, V.; Wolf, W.; Reith, D.; Rozanska, X.; Freeman, C.; Saxe, P. Computational Materials Engineering: Recent Applications of VASP in the MedeA® Software Environment. *J. Korean Ceram. Soc.* **2016**, *53*, 263–272. [[CrossRef](#)]
39. Hafner, J.; Kresse, G. The Vienna AB-Initio Simulation Program VASP: An Efficient and Versatile Tool for Studying the Structural, Dynamic, and Electronic Properties of Materials. In *Properties of Complex Inorganic Solids*; Springer: Boston, MA, USA, 1997; pp. 69–82. [[CrossRef](#)]
40. Perdew, J.P.; Burke, K.; Ernzerhof, M. Generalized Gradient Approximation Made Simple. *Phys. Rev. Lett.* **1996**, *77*, 3865–3868. [[CrossRef](#)]
41. Becke, A.D. Density-functional thermochemistry. III. The role of exact exchange. *J. Chem. Phys.* **1993**, *98*, 5648–5652. [[CrossRef](#)]
42. Pavone, M.; Ritzmann, A.; Carter, E.A. Quantum-mechanics-based design principles for solid oxide fuel cell cathode materials. *Energy Environ. Sci.* **2011**, *4*, 4933–4937. [[CrossRef](#)]
43. Dudarev, S.L.; Botton, G.A.; Savrasov, S.Y.; Humphreys, C.J.; Sutton, A.P. Electron-energy-loss spectra and the structural stability of nickel oxide: An LSDA+U study. *Phys. Rev. B* **1998**, *57*, 1505–1509. [[CrossRef](#)]

44. Muñoz-García, A.B.; Sannino, F.; Vitiello, G.; Pirozzi, D.; Minieri, L.; Aronne, A.; Pernice, P.; Pavone, M.; D'Errico, G. Origin and Electronic Features of Reactive Oxygen Species at Hybrid Zirconia-Acetylacetonate Interfaces. *ACS Appl. Mater. Interfaces* **2015**, *7*, 21662–21667. [[CrossRef](#)] [[PubMed](#)]
45. Muñoz-García, A.B.; Tuccillo, M.; Pavone, M. Computational design of cobalt-free mixed proton–electron conductors for solid oxide electrochemical cells. *J. Mater. Chem. A* **2017**, *5*, 11825–11833. [[CrossRef](#)]
46. Tuccillo, M.; Palumbo, O.; Pavone, M.; Muñoz-García, A.B.; Paolone, A.; Brutti, S. Analysis of the Phase Stability of LiMO₂ Layered Oxides (M = Co, Mn, Ni). *Crystals* **2020**, *10*, 526. [[CrossRef](#)]
47. Bader, R.F.W. *Atoms in Molecules: A Quantum Theory*; Oxford University Press: Oxford, UK, 1990; 438p.
48. Sanville, E.; Kenny, S.D.; Smith, R.; Henkelman, G. Improved grid-based algorithm for Bader charge allocation. *J. Comput. Chem.* **2007**, *28*, 899–908. [[CrossRef](#)] [[PubMed](#)]
49. Tang, W.; Sanville, E.; Henkelman, G. A grid-based Bader analysis algorithm without lattice bias. *J. Phys. Condens. Matter* **2009**, *21*, 084204. [[CrossRef](#)] [[PubMed](#)]
50. Zunger, A.; Wei, S.-H.; Ferreira, L.G.; Bernard, J.E. Special quasirandom structures. *Phys. Rev. Lett.* **1990**, *65*, 353. [[CrossRef](#)]
51. Massaro, A.; Muñoz-García, A.B.; Prosini, P.P.; Gerbaldi, C.; Pavone, M. Unveiling Oxygen Redox Activity in P2-Type Na_xNi_{0.25}Mn_{0.68}O₂ High-Energy Cathode for Na-Ion Batteries. *ACS Energy Lett.* **2021**, *6*, 2470–2480. [[CrossRef](#)]
52. Mayer, J.E.; Montroll, E. Molecular Distribution. *J. Chem. Phys.* **1941**, *9*, 2–16. [[CrossRef](#)]
53. Van de Walle, A.; Asta, M.; Ceder, G. The alloy theoretic automated toolkit: A user guide. *Calphad* **2002**, *26*, 539–553. [[CrossRef](#)]
54. Nayak, P.K.; Grinblat, J.; Levi, M.; Aurbach, D. Electrochemical and structural characterization of carbon coated Li_{1.2}Mn_{0.56}Ni_{0.16}Co_{0.08}O₂ and Li_{1.2}Mn_{0.6}Ni_{0.2}O₂ as cathode materials for Li-ion batteries. *Electrochim. Acta* **2014**, *137*, 546–556. [[CrossRef](#)]
55. Wu, F.; Kim, G.; Kuenzel, M.; Zhang, H.; Asenbauer, J.; Geiger, D.; Kaiser, U.; Passerini, S. Elucidating the Effect of Iron Doping on the Electrochemical Performance of Cobalt-Free Lithium-Rich Layered Cathode Materials. *Adv. Energy Mater.* **2019**, *9*, 1902445. [[CrossRef](#)]
56. Simonelli, L.; Sorrentino, A.; Marini, C.; Ramanan, N.; Heinis, D.; Olszewski, W.; Mullaliu, A.; Birrozzi, A.; Laszczynski, N.; Giorgetti, M.; et al. Role of Manganese in Lithium- and Manganese-Rich Layered Oxides Cathodes. *J. Phys. Chem. Lett.* **2019**, *10*, 3359–3368. [[CrossRef](#)] [[PubMed](#)]
57. Jin, Y.; Xu, Y.; Sun, X.; Xiong, L.; Mao, S. Electrochemically active MnO₂ coated Li_{1.2}Ni_{0.18}Co_{0.04}Mn_{0.58}O₂ cathode with highly improved initial coulombic efficiency. *Appl. Surf. Sci.* **2016**, *384*, 125–134. [[CrossRef](#)]
58. Wu, F.; Kim, G.; Diemant, T.; Kuenzel, M.; Schür, A.R.; Gao, X.; Qin, B.; Alwast, D.; Jusys, Z.; Behm, R.J.; et al. Reducing Capacity and Voltage Decay of Co-Free Li_{1.2}Ni_{0.2}Mn_{0.6}O₂ as Positive Electrode Material for Lithium Batteries Employing an Ionic Liquid-Based Electrolyte. *Adv. Energy Mater.* **2020**, *10*, 2001830. [[CrossRef](#)]
59. Shannon, R.D.; Prewitt, C.T. Effective ionic radii in oxides and fluorides. *Acta Cryst.* **1969**, *25*, 925–946. [[CrossRef](#)]
60. Kugel, K.; I Khomskii, D. The Jahn-Teller effect and magnetism: Transition metal compounds. *Sov. Phys. Uspekhi* **1982**, *25*, 231. [[CrossRef](#)]
61. Voronina, N.; Sun, Y.-K.; Myung, S.-T. Co-Free Layered Cathode Materials for High Energy Density Lithium-Ion Batteries. *ACS Energy Lett.* **2020**, *5*, 1814–1824. [[CrossRef](#)]
62. Nakamura, T.; Gao, H.; Ohta, K.; Kimura, Y.; Tamenori, Y.; Nitta, K.; Ina, T.; Oishi, M.; Amezawa, K. Defect chemical studies on oxygen release from the Li-rich cathode material Li_{1.2}Mn_{0.6}Ni_{0.2}O₂– δ . *J. Mater. Chem. A* **2019**, *7*, 5009–5019. [[CrossRef](#)]
63. Longuet-Higgins, H.C.; Opik, U.; Pryce, M.H.L.; Sack, R.A. Studies of the Jahn-Teller effect. II. The dynamical problem. *Proc. R. Soc. Lond. Ser. A Math. Phys. Sci.* **1958**, *244*, 1–16. [[CrossRef](#)]
64. Tan, S.; Zhang, Z.; Li, Y.; Li, Y.; Zheng, J.; Zhou, Z.; Yang, Y. Tris (hexafluoro-iso-propyl) phosphate as an SEI-Forming Additive on Improving the Electrochemical Performance of the Li[Li_{0.2}Mn_{0.56}Ni_{0.16}Co_{0.08}]O₂ Cathode Material. *J. Electrochem. Soc.* **2012**, *160*, A285. [[CrossRef](#)]
65. Sun, Y.-K. Structural degradation mechanism of oxysulfide spinel LiAl_{0.24}Mn_{1.76}O_{3.98}S_{0.02} cathode materials on high temperature cycling. *Electrochem. Commun.* **2001**, *3*, 199–202. [[CrossRef](#)]
66. Mohanty, D.; Huq, A.; Payzant, E.A.; Sefat, A.S.; Li, J.; Abraham, D.P.; Wood, D.; Daniel, C. Neutron Diffraction and Magnetic Susceptibility Studies on a High-Voltage Li_{1.2}Mn_{0.55}Ni_{0.15}Co_{0.10}O₂ Lithium Ion Battery Cathode: Insight into the Crystal Structure. *Chem. Mater.* **2013**, *25*, 4064–4070. [[CrossRef](#)]
67. Celeste, A.; Tuccillo, M.; Santoni, A.; Reale, P.; Brutti, S.; Silvestri, L. Exploring a Co-Free, Li-Rich Layered Oxide with Low Content of Nickel as a Positive Electrode for Li-Ion Battery. *ACS Appl. Energy Mater.* **2021**, *4*, 11290–11297. [[CrossRef](#)]